NANO LETTERS
Letter
pubs.acs.org/NanoLett

Revealing Grain-Boundary-Induced Degradation Mechanisms in Li-Rich Cathode Materials

Soroosh Sharifi-Asl,[†] Vitaliy Yurkiv,[†] Arturo Gutierrez,[‡] Meng Cheng,[†] Mahalingam Balasubramanian,[§] Farzad Mashayek,[†] Jason Croy,[*,‡] and Reza Shahbazian-Yassar[*,†]

[†]Mechanical and Industrial Engineering Department, University of Illinois at Chicago, Chicago, Illinois 60607, United States
[‡]Chemical Science and Engineering, Argonne National Laboratory, Argonne, Illinois 60561, United States
[§]Advanced Photon Source, Argonne National Laboratory, Argonne, Illinois 60561, United States

Supporting Information

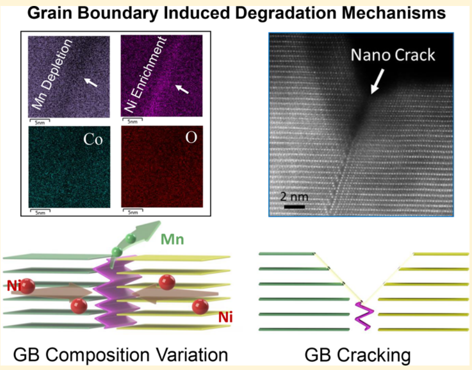

ABSTRACT: Despite their high energy densities, Li- and Mn-rich, layered−layered, $x\mathrm{Li_2MnO_3}\cdot(1-x)\mathrm{LiTMO_2}$ (TM = Ni, Mn, Co) (LMR-NMC) cathodes require further development in order to overcome issues related to bulk and surface instabilities such as Mn dissolution, impedance rise, and voltage fade. One promising strategy to modify LMR-NMC properties has been the incorporation of spinel-type, local domains to create "layered−layered−spinel" cathodes. However, precise control of local structure and composition, as well as subsequent characterization of such materials, is challenging and elucidating structure−property relationships is not trivial. Therefore, detailed studies of atomic structures within these materials are still critical to their development. Herein, aberration corrected-scanning transmission electron microscopy (AC-STEM) is utilized to study atomic structures, prior to and subsequent to electrochemical cycling, of LMR-NMC materials having integrated spinel-type components. The results demonstrate that strained grain boundaries with various atomic configurations, including spinel-type structures, can exist. These high energy boundaries appear to induce cracking and promote dissolution of Mn by increasing the contact surface area to electrolyte as well as migration of Ni during cycling, thereby accelerating performance degradation. These results present insights into the important role that local structures can play in the macroscopic degradation of the cathode structures and reiterate the complexity of how synthesis and composition affect structure−electrochemical property relationships of advanced cathode designs.

KEYWORDS: *Li-ion battery, Li-rich cathodes, layered oxide cathodes, structural degradation, grain boundary, STEM/EELS*

Layered, LiTMO$_2$-type cathode-oxides are the dominant positive electrodes in commercial Li-ion battery (LIB) technologies. Such materials have been aggressively developed and are now nearing the point of intrinsic limitation, thereby hindering further advancements.[1] Li-rich, LMR-NMC cathodes, that can deliver capacities between 250−300 mAhg^{-1}, are considered promising options for the next generation of LIBs.[2,3] However, the practical application of Li-rich materials has been challenging due to several phenomena that are unique to these oxides, namely, voltage fade, hysteresis, and impedance at low states of charge (SOC).[4−9] The mechanisms behind these phenomena are unique to these oxides because of the complexity of their local structures, and recent works have made progress with respect to understanding in this regard.[6,10,11] However, as with all cathode-oxides, macroscopic phenomena can also play a critical role in performance. For example, cracking and disintegration of secondary macro-particles, which are agglomerates of primary cathode grains, have been correlated with severe capacity degradation.[12] It has been demonstrated that the lithiation/delithiation process induces contraction/expansion of the crystal structure, which leads to large strain in the primary particles and promotes the disintegration and cracking of secondary particles.[13] In addition, surface degradation such as layered-to-spinel-to-disordered rock-salt transformations, as well as transition metal migration/dissolution, have been observed in virtually all conventional, layered oxides.[14−18]

In LMR-NMC cathodes, it has been shown that even a small concentration of local defects can greatly influence the macroscopic electrochemical properties of cathode electrodes.[19,20] However, to what extent the atomic-scale structure can affect properties such as particle cracking/disintegration, in complex LMR-NMC-based particles, is not well-understood. Recent work, using operando X-ray tomography, has reported that charging LMR-NMCs induces a high extent of defects, consistent with previous findings, which is not observed in

Received: November 8, 2019
Revised: December 22, 2019
Published: December 23, 2019

DOI: 10.1021/acs.nanolett.9b04620

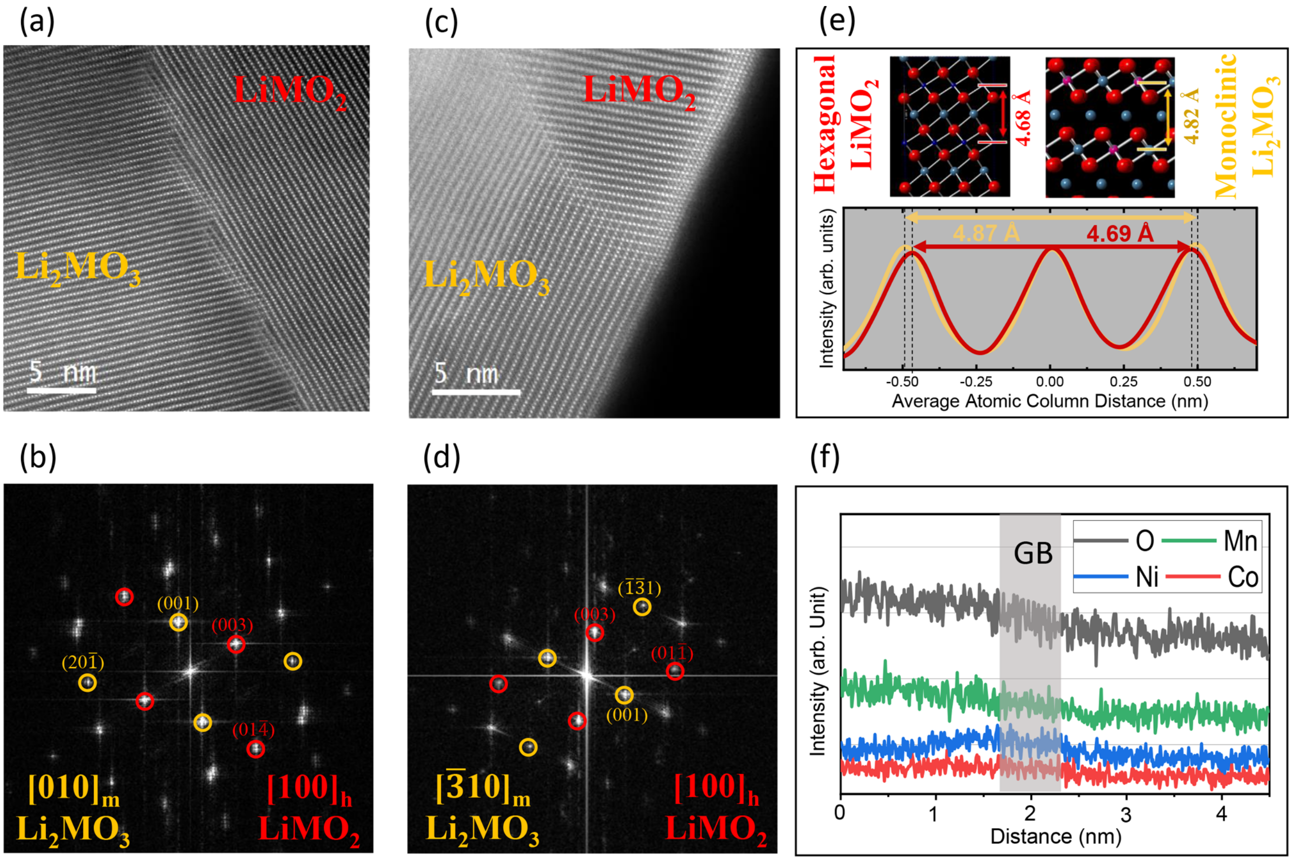

Figure 1. (a–d) Atomic resolution HAADF images and the corresponding FFT patterns from the core of an LMR-NMC particle showing a boundary between two layered phases. FFT analysis reveals that the observed layered phases shown in panels a and c correspond to the [010] and [$\bar{3}$10] projections of the monoclinic Li_2MO_3 phase and the [100] projection of the hexagonal $LiMO_2$ phase, respectively. (e) Line profile analysis from the interlayer distances observed in part a. Yellow and red profiles correspond to the monoclinic and hexagonal phases, respectively. The plot illustrates a 0.2 Å increase in the interlayer distance in the monoclinic-labeled phase compared to the hexagonal phase, which is in accordance with the atomic models shown above. (f) The EDS line scan taken across a $LiMO_2/Li_2MnO_3$ grain boundary shown in Figure S3.

conventional cathodes such as $Li(Ni_xCo_yAl_{1-x-y})O_2$ (NCA).[21] In that work, the authors hypothesize that the lower Young's modulus of the Li-rich materials[21] is the underlying cause for defect formation/activity, although an atomic-scale analysis that explains such results is still lacking. Furthermore, though the pristine structure of LMR-NMCs has been the subject of extensive study and debate,[21−30] the atomic arrangement of the phase boundaries in these structures and how those boundaries change during cycling have not been thoroughly investigated.

Herein, we have used aberration corrected-scanning transmission electron microscopy (AC-STEM) to investigate the atomic structure and chemistry of a Li-rich, layered−layered−spinel material before and after electrochemical cycling. Our findings directly indicate that the primary cathode particles are composed of distinct, randomly oriented nanograins of hexagonal $LiTMO_2$ and monoclinic Li_2TMO_3 structures (TM = Co, Ni, and Mn). Hence, high concentrations of phase/grain boundaries were detected in the structures of these cathodes. Based on the geometrical phase analysis (GPA), such phase boundaries are highly strained, which can cause cracking and disintegration of particles during repeated electrochemical cycling. In addition, chemical analysis, through electron dispersive spectroscopy (EDS) and electron energy loss spectroscopy (EELS), suggests a uniform composition across the boundaries in the pristine samples. However, Mn depletion and Ni enrichment were detected in the boundaries of cycled samples. Additionally, crack initiation was observed in the phase boundaries after extended cycling, which implies that grain/phase boundaries play a detrimental role in the structural stability of the Li-rich cathode materials. Finally, density function theory (DFT) investigations were conducted in order to better understand the underlying reasons for composition variation of the grain boundaries.

Results. The details of sample synthesis, basic characterization, and electrochemical tests are provided in the Supporting Information. TEM analysis has been carried out on the surface and the core of cathode particles to study their atomic structure. The individual nanoparticles, separated by means of ultrasonication and dispersed on the TEM grids, are thin enough at the surface and core areas to be electron transparent (Figure S2). High-angle annular dark field imaging (HAADF), which is a *Z*-contrast imaging technique[31] and is capable of detecting transition metal atoms (but cannot distinguish between Mn, Ni, and Co with very close atomic numbers), has been used as the primary imaging technique in this research. In addition, low-angle annular dark field (LAADF) imaging, that is principally used for defect imaging,[32] is used as a complementary technique to HAADF.

By examining the pristine cathode samples, it was realized that the primary particles are composed of layered-structured grains with varied orientations with respect to each other (Figure 1a,b). The corresponding fast Fourier transformed

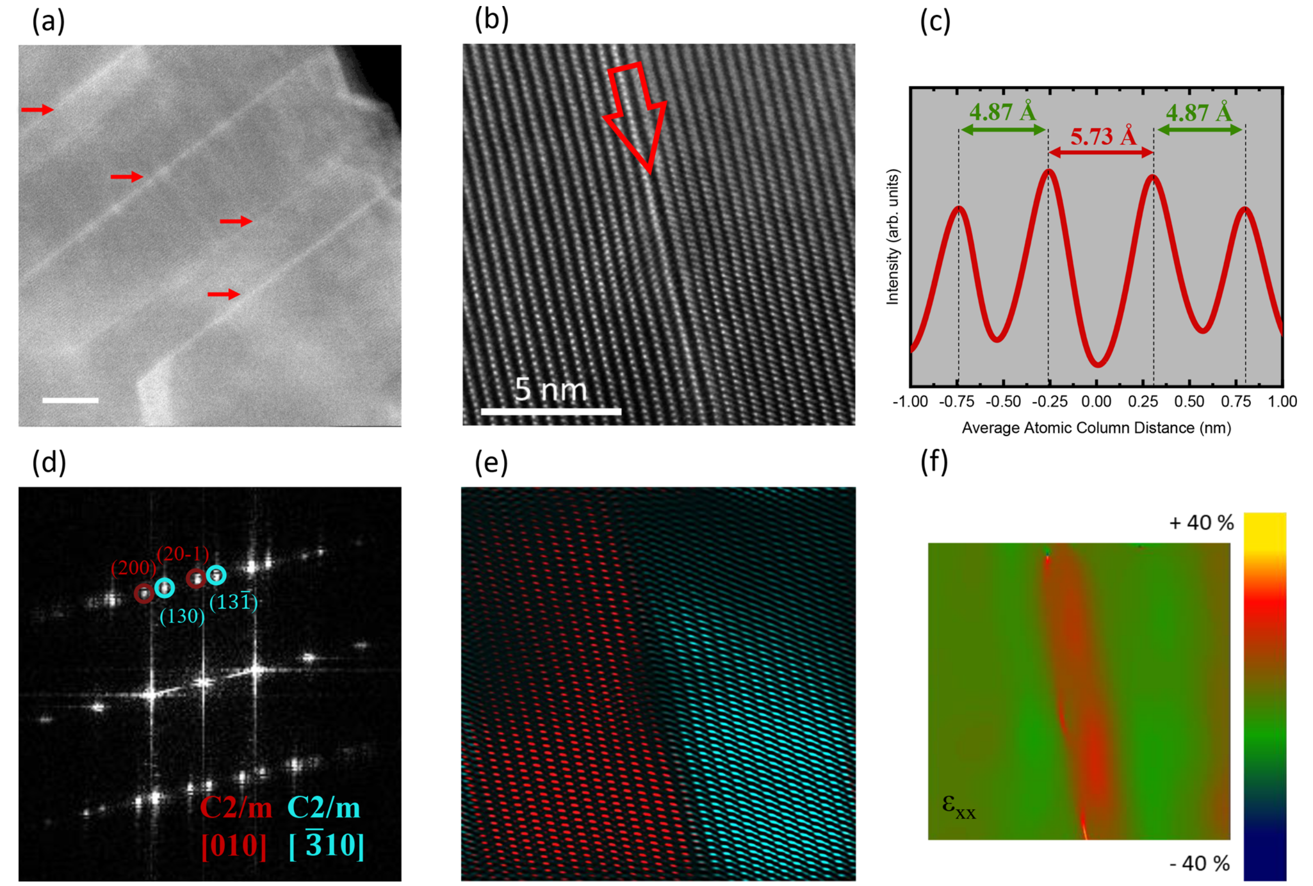

Figure 2. (a) Low magnification LAADF image from a pristine cathode particle showing a high concentration of elongated defects as indicated by red arrows. (b) Atomic resolution HAADF image from a line-defect indicated in part a. Based on the (c) line profile measurement and (d) FFT analysis, the defect is an elongated interlayer distance where [010] and $[\bar{3}10]$ projections of monoclinic Li_2MO_3 phases are forming a grain boundary. (e) Reconstructed color-coded image from the indicated diffraction spots in part d illustrating the separation of two grains. (f) GPA results showing a large strain in the grain boundary as a result of increased interlayer distance.

(FFT) images are shown in Figure 1c,d. Based on the FFT analysis, it can be concluded that the two intersecting grains correspond to [010] and $[\bar{3}10]$ projections of the monoclinic Li_2MO_3 phase and the [100] projection of the hexagonal $LiMO_2$ phase, respectively. In addition to FFT analysis, the interlayer distances of the layered structures in Figure 1c are quantified through line profile measurements and the results are demonstrated in Figure 1e. The yellow and red profiles correspond to the monoclinic and hexagonal phases, respectively. It can be observed that the interlayer distances of the monoclinic-labeled structure are ca. 0.2 Å larger, which is in accordance with the atomic models. Although such projections from the monoclinic and hexagonal phases have a very close atomic configuration and interlayer distances, such small variations can be quantified through sub-angstrom AC-STEM imaging. In addition, chemical composition analysis using EDS and EELS was carried out as a complementary technique to verify the coexistence of monoclinic Li_2MO_3 and hexagonal $LiMO_2$ phases. Figure 1e demonstrates an EDS line scan collected across a grain boundary between Li_2MO_3 and $LiMO_2$ grains (Figure S3a). In spite of a very small variation in the transition metal signals, a considerable reduction in O signal intensity can be observed by moving from the Li_2MO_3 grain to the $LiMO_2$ grain.

Further investigations of the grain boundaries in the pristine cathode particles were carried out by defect-sensitive LAADF and atomic resolution imaging. Figure 2a demonstrates a low-magnification LAADF image from a pristine particle. The high contrast lines, indicated with red arrows, correspond to defects in the structure. Considering the 50 nm width of the image, the presence of four line-defects demonstrates a high concentration of defects in this particle. Atomic resolution imaging reveals that the bright elongated lines in the LAADF correspond to an increased interlayer distance in the layered structure of the sample (Figure 2b). As shown in Figure 2c, the interlayer distance has increased from 4.87 Å in the adjacent area to 5.73 Å in the defect line. Based on the FFT pattern analysis shown in Figure 2d, it is concluded that the increased interlayer distance corresponds to a grain boundary between [010] and $[\bar{3}10]$ projections of the monoclinic structure. Figure 2e demonstrates the color-coded reconstructed image based on the FFT pattern, illustrating the presence of various projections of the monoclinic phase in this area. Moreover, GPA was carried out on the atomic resolution image in Figure 2b, which demonstrates a large strain in the grain boundary (Figure 2f). The observed strain is generated as a result of the increased interlayer distance in the grain boundary, which can possibly lead to cracking, impedance rise, and capacity fade of the battery during electrochemical cycling.

A different configuration of grain boundaries is shown in Figure 3a, where dissimilar projections of the monoclinic structure are facing each other. Although there is a one-to-one

DOI: 10.1021/acs.nanolett.9b04620

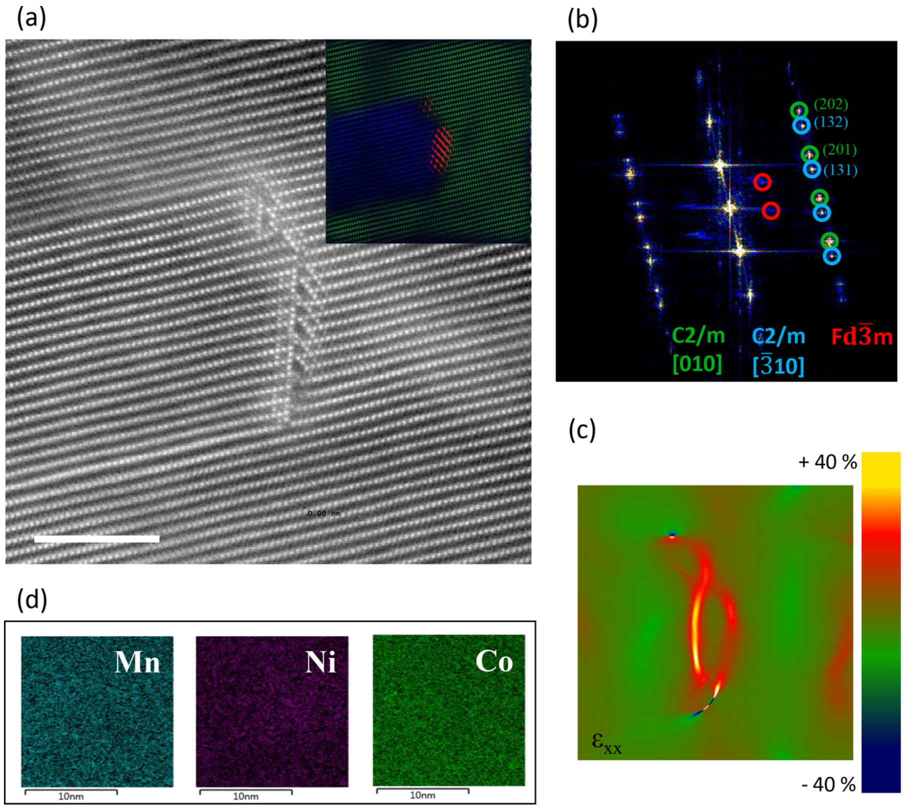

Figure 3. (a) The atomic resolution HAADF image from a pristine cathode particle, showing a spinel-type grain boundary. (b) The corresponding FFT image demonstrating the presence of the [010] and [$\bar{3}$10] projections of the monoclinic Li_2MO_3 phase and formation of the spinel-type structure at the grain boundary as a result of migration of transition metals to the Li-octahedral sites. A color-coded reconstruction image based on the diffraction spots indicated in part b is shown as the inset in part a for illustration of the triple phase boundary. (c) GPA, showing a large strain in the spinel-type grain boundary. (d) EDS maps of Mn, Ni, and Co from the grain boundary confirming a uniform composition at the grain boundary.

correspondence between the atomic layers of [010] and [$\bar{3}$10] phases, a distinct spinel-type grain boundary is formed that is a result of transition metal migration to the Li-octahedral sites. Such transition metal migration has occurred in one to two unit cells that are adjacent to the grain boundary. Figure 3b demonstrates the corresponding FFT pattern, which is analyzed as a three-phase structure consisting of [010] and [$\bar{3}$10] projections of the monoclinic Li_2MO_3 structure, plus the spinel-type interface. A color-coded reconstructed image is shown as an inset in Figure 3a for illustration of grain configurations. As can be seen from the GPA shown in Figure 3c, such spinel-type grain boundaries are also highly strained and may also act as crack and failure initiation points in the cycled material. In addition, chemical analysis has been carried out on the spinel-type grain boundary area by EDS, shown in Figure 3d. Although the results demonstrate that the distribution of Mn, Ni, and Co appears to be uniform in both surrounding monoclinic Li_2MO_3 grains[29] as well as across the boundary, it should be noted that we cannot rule out the Li−Mn ordering and formation of $LiMn_6$- and $LiMn_5Ni_1$-type structures in the subnano scale, reported through XAS and NMR studies.[33−36] However, resolving such angstrom scale chemical deviations was beyond the spatial resolution achievable in our case due to signal averaging in the cross section of the sample.

To understand the role of the identified grain/phase boundaries on the electrochemical degradation structural stability of the particles, AC-STEM experiments were carried out on the cycled cathode particles. Figure 4a demonstrates an LAADF image from a cycled cathode particle with bright contrast features that correspond to the identified grain/phase boundaries. Figure 4b is an atomic resolution image from the indicated area in the low-magnification image, which demonstrates a spinel-type grain boundary with the same grain configuration as was observed in the pristine particle shown in Figure 3. The phase transition at the surface regions of the particle can be observed, which is an expected phenomenon in the cycled layered oxide cathodes.[37,38] Additionally, it can be observed that a nanocrack has initiated on the grain boundary, which might develop into a more significant crack and initiate disintegration of the cathode upon further cycling. The analyzed FFT pattern demonstrates that the spinel-type boundary is located between the [010] and [$\bar{3}$10] projections of the monoclinic Li_2MO_3 phase, similar to the atomic configuration observed in the pristine sample. The color-coded reconstructed image, Figure 4d, illustrates the configuration of the identified grains and the spinel-type grain boundary. Aside from the layered to spinel/rock-salt phase transformation that can be observed in the surface areas of both grains and transition metal migration to Li sites, stacking fault disorder can be detected in the cycled sample. Figure 4e shows an atomic resolution image from the [010] grain located on the right side of Figure 4b, demonstrating a disorder in the stacking of the layers. The stacking faults, induced by slab sliding during electrochemical cycling, denote the electrochemical activity present in the Li-rich domains. Figure 4f

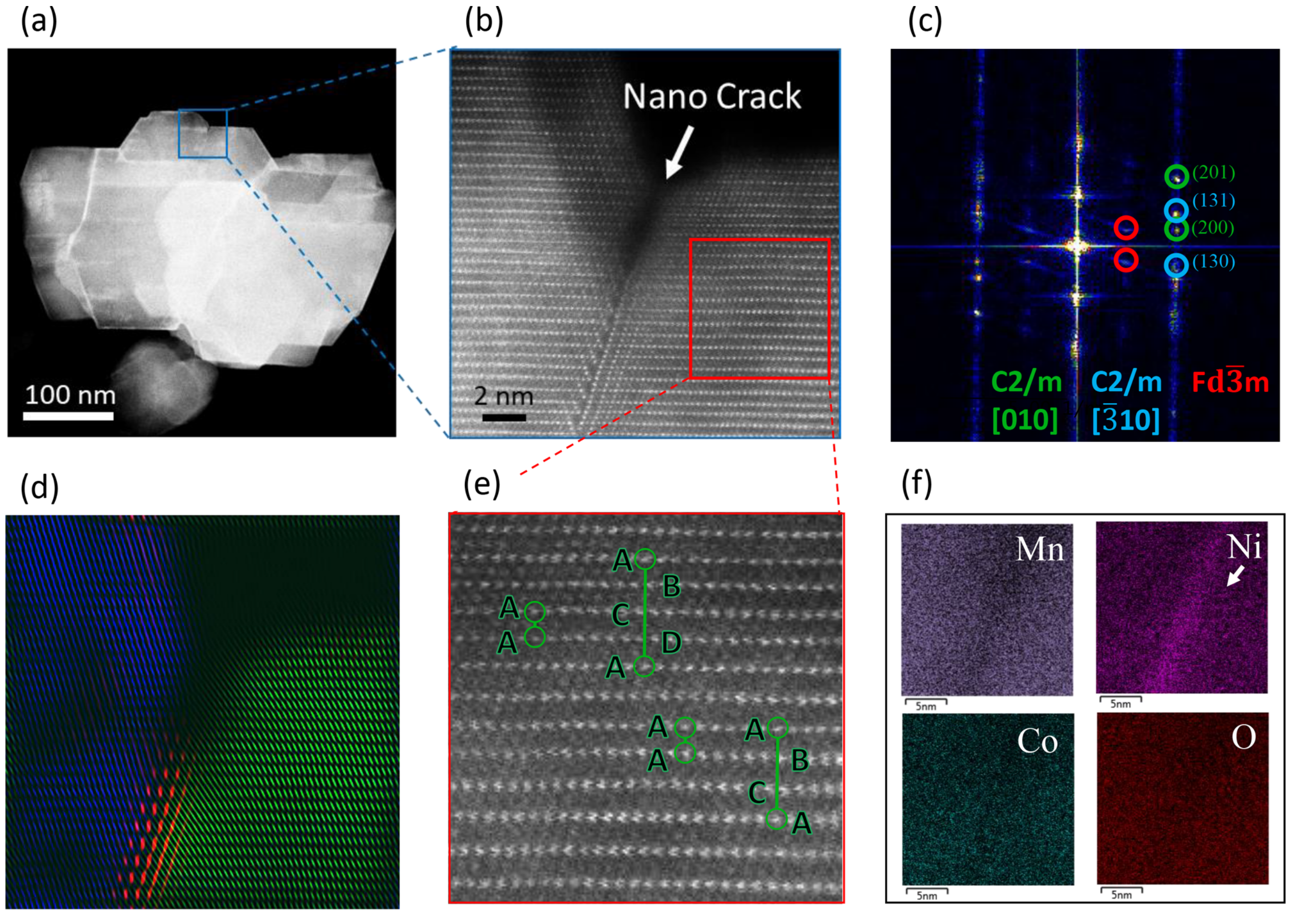

Figure 4. (a) Low-magnification LAADF image showing a cycled cathode particle. Various bright contrast features can be observed in the particle which can be attributed to previously shown grain/phase boundaries. (b) Atomic resolution HAADF image from the indicated area in part a, which shows a spinel-type grain boundary that forms a nanocrack at the particle surface. (c) The corresponding FFT pattern that is indexed as a three-phase structure consisting of [010] and $[\bar{3}10]$ projections of the Li$_2$MO$_3$ structure together with the spinel-type boundary, similar to the atomic configuration of the pristine sample. (d) Color-coded reconstructed image, based on the indicated diffraction spots in part c, illustrating the three-phase structure of the imaged area. (e) Atomic resolution image from the [010] projection on the right side of part b, showing a disorder in the stacking of the layers. (f) EDS maps obtained from the spinel-type grain boundary showing the depletion of Mn and enrichment of Ni in the grain boundary subsequent to the electrochemical cycling.

demonstrates EDS map results from the indicated spinel-type boundary, which shows localized depletion of Mn and enrichment of Ni at the boundary. The localized chemical inhomogeneity in the interface is only observed after electrochemical cycling of the particles. The depletion of Mn may be attributed to a preferred dissolution of Mn from high energy grain boundaries that subsequently promotes the diffusion of Ni into the Mn/Li vacancies, as discussed below. The increased dissolution of Mn and increased Ni migration to the grain boundary can also be the result of cracking of the particle surface and exposing new surfaces to the electrolyte, which promotes the metal dissolution. The promoted metal dissolution can, in turn, negatively affect cell performance through Mn deposition and Li consumption at the graphite anode as well as impedance rise at the now disordered cathode surface.[39,40] In addition, crack formation, exposure of fresh particle surfaces, and eventual disintegration of the active materials serve to exacerbate these problems.

The increased Ni concentration at the grain boundary has also been confirmed by EELS. Figure 5a demonstrates an atomic resolution HAADF image from a grain boundary on a cycled cathode particle. An EELS map was acquired from the grain boundary and the signal from an equal number of pixels in the spinel-type grain boundary, and the adjacent layered areas were summed and compared as shown in Figure 5b. It can be clearly observed that the grain boundary shows a less intense Mn signal. However, the Ni concentration has increased, while, interestingly, the Co content has remained almost the same, consistent with EDS results on a different particle (Figure 4f). It should be noted that, while the intensity of the Ni L$_3$ edge at 851 eV has substantially increased at the grain boundary, the L$_2$ edge at 870 eV has a very similar intensity in both spectra. This increase in the relative intensity of Ni L$_3$/L$_2$ edges denotes the reduction of the valence state and change in the Ni bonding at the interface.[41] The increased Ni concentration in the spinel-type boundaries could also be explained by the preferred migration of Ni cations into the Li layers that forms these structures. Preferred migration of Ni ions into Li vacancies has been observed in conventional NMC cathodes via electron microscopy and X-ray spectroscopy.[38,39,42] Moreover, segregation of Ni and Co has been observed at specific facet terminations in the Li-rich cathode materials.[38] However, it is interesting that here we observe such phenomena at complex interfaces within these materials.

To understand the atomic interactions that promote preferred Ni migration to the grain boundaries, complementary

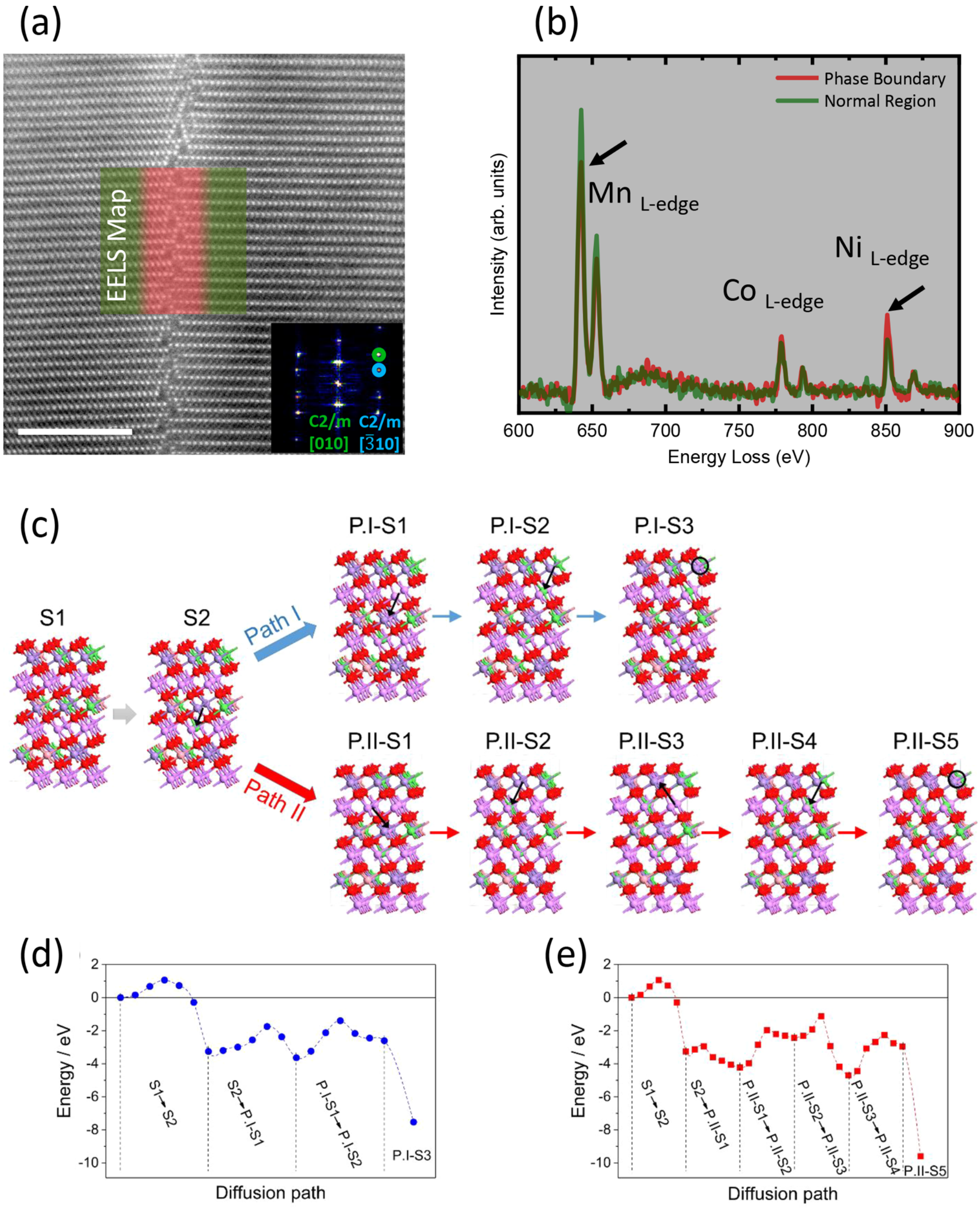

Figure 5. (a) HAADF atomic resolution image from a grain boundary in the bulk structure of a cycled LMR-NMC particle sample. (b) EELS spectra showing the Co and Ni L edges from the specified area in part a. Increased Ni concentration can be observed at the grain boundary area. (c) Two paths (path I and path II) of Li/Ni exchange. Path I (upper panel) depicts the "direct" (shortest distance) Li/Ni exchange. Path II (lower panel) shows the "side" Li/Ni exchange. The first two slabs on the left are the same for both paths. (d and e) The energetics and the migration barriers of Li and Ni atoms for path I and path II as obtained in the present DFT calculations.

DFT calculations were performed and favorable pathways for Li/M (M = Ni, Mn, and Co) exchange in the cathode structure were studied. Several configurations varying the Ni, Mn, and Co position within the simulated slab were considered (Figure S4). Among many possible calculated structures, a structure with Ni segregation in the grain boundary was revealed to be the most stable. In addition, the diffusion of all three transition metal atoms into Li vacancies is calculated and compared. It was found that diffusion of Ni ions into the Li vacancies (Figure 5c−e) was the most favorable process when compared to Mn and Co (Figures S5 and S6). These results agree with the experimentally observed Ni accumulation within the grain boundaries.

Additional DFT calculations have been carried out to elucidate the details of the observed Ni migration to Li vacancies. Two possible pathways for migration are identified, referred to as path I and path II, and are illustrated in Figure 5c. Both pathways start with the same atomic configuration (namely, S1), where the indicated Ni atom diffuses to the nearest Li vacancy, leaving a Ni vacancy and forming the S2 configuration. This process is energetically favorable by 3.1 eV, as shown in Figure 5d and e, where the energies of all diffusion pathways are shown. Subsequent Li diffusion into the Ni vacancy in configuration S2 could occur from two nearest neighbors. Path I depicts a "direct" exchange of Ni/Li vacancy, and path II corresponds to a "side" exchange. Path I describes the Li atom diffusion from the nearest neighbor on the right,

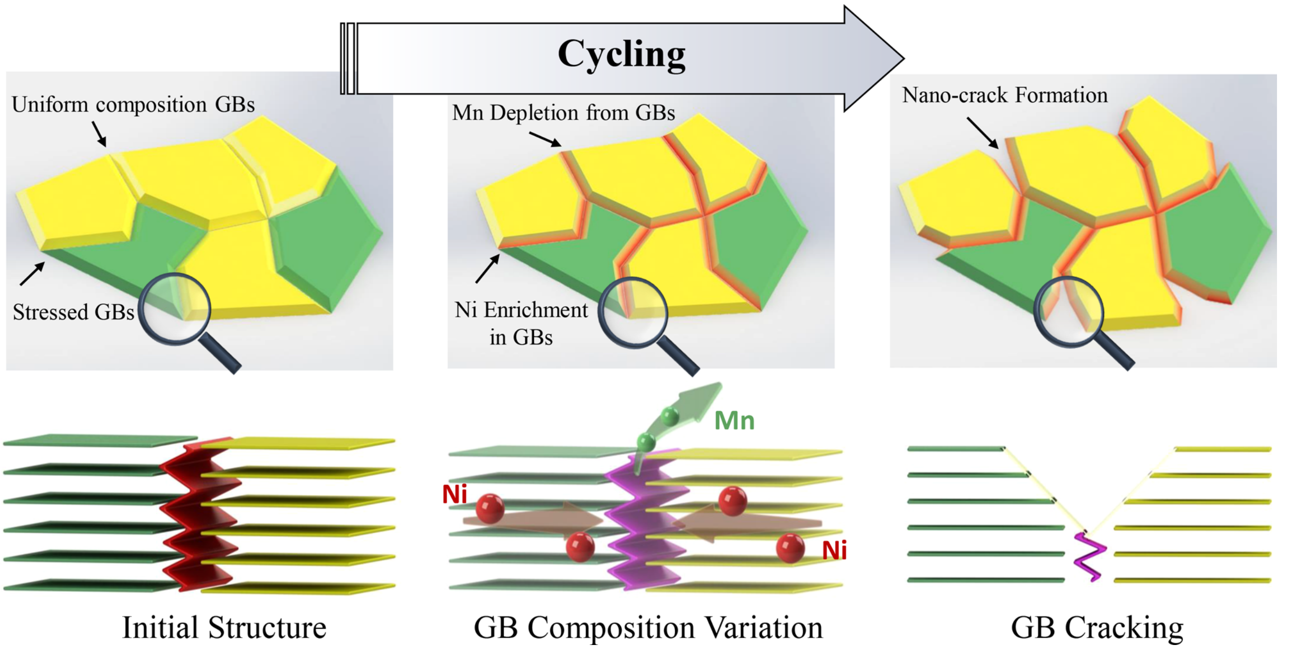

Figure 6. Schematic illustration of the proposed grain-boundary-induced degradation mechanisms in Li-rich cathodes. During cycling, the grain boundaries are depleted of Mn and enriched in Ni, possibly aiding in crack initiation at the already strained grain boundaries.

while path II shows the Li atom diffusion from the nearest neighbor on the left. The Li atom diffusion in path II is more energetically favorable (Δh = −0.97 eV) with a smaller activation barrier (E^{act} = 0.3 eV) than the respective Li atom diffusion of path I (Δh = −0.38 eV and E^{act} = 0.7 eV). In either case, the creation of a Li vacancy leads to the P.I−S1 and P.II−S1 configurations. The processes P.I−S1 to P.I−S2 in path I and P.II−S1 to P.II−S2 in path II describe Ni diffusion from either side of the Li vacancy. This process is energetically unfavorable in both paths (path I, Δh = +1.03 eV and E^{act} = 2.24 eV; path II, Δh = +1.79 eV and E^{act} = 2.25 eV). However, the consequent Li atom diffusion into the metal vacancy is highly favorable, having Δh = −4.92 eV in path I and Δh = −2.27 eV in path II. The large difference between the enthalpies in the last step in path I and path II is because a Li atom is inserted into the metal vacancy, since there is no further Li atom in the slab. The corresponding insertion in path II is shown by the P.II−S6 structure, where the enthalpy difference is Δh = −6.64 eV. This process, of Ni migration, can progress along the bulk structure of NMC creating defects or contributing to crack initiation within the electrode.

In conclusion, aberration corrected-scanning transmission electron microscopy was performed on the bulk structure of Li-rich cathode materials having integrated spinel-type domains. The complex atomic structure of grain/phase boundaries that can form in the LMR-NMC cathode materials was identified. The presented atomic study, which was enabled by synthesis of thin, electron transparent cathode particles, demonstrated the presence of a layered−layered, hexagonal−monoclinic structure with various possible grain/phase boundary structures, such as spinel interfaces. These structures were found to have a dependence on the configuration of the adjacent grains, where stacking of two layered grains perpendicular to their layered structure formed grain boundaries with increased interlayer distances, whereas stacking of grains parallel to their layered structures resulted in a spinel-type grain boundary. It was demonstrated that such grain boundaries, that are also highly strained, would promote initiation of crack formation. Subsequently, fracture and disintegration of the active materials may ensue, resulting in loss of performance. Additionally, Mn depletion and Ni enrichment were observed in the grain boundaries of cycled samples, implying an important role of such boundaries in performance degradation mechanisms. Such grain-boundary-induced degradation mechanisms are schematically depicted in Figure 6. The underlying reason for atomic migration of Ni into spinel-type grain boundaries was investigated using DFT calculations. Among the various calculated structures, a configuration with Ni migration into Li vacancies was revealed to be the most energetically favorable structure, correlating well with the experimental observations. This work reveals the complex role between composition, synthesis, and structure−property relationships of advanced cathode designs and reiterates the important role that local atomic structures can play in defining macroscopic electrode properties as well as the need to further understand these materials across various length scales.

Experimental Section. *Synthesis of Cathode Particles.* A coprecipitation process was used to synthesize Ni−Mn−Co (NMC) carbonate precursors using a 4 L continuously stirred tank reactor (CSTR). An initial volume of 3 L of DI water was used. The CSTR was sealed, and N_2 was flowed to remove air and avoid oxidation of the product. Stock solutions of ammonium hydroxide (0.05 M NH_4OH), sodium carbonate (2 M Na_2CO_3), and NMC sulfate (2 M NMC−SO_4) were pumped into the tank to allow for a 6 h residence time. The reaction was stopped after 24 h (four residence times), and the product was filtered, washed, and then dried overnight at 110 °C. The NMC-carbonate was then mixed with the appropriate amount of lithium carbonate and fired at 900 °C (2 °C/min) for 20 h. The “parent” LMR-NMC material for this work is based on the following composition: $0.25Li_2MnO_3 \cdot 0.75LiMO_2$ or $Li_{1.25}Mn_{0.53}Ni_{0.28}Co_{0.19}O_x$, where Li/TM = 1.25. In order to integrate a spinel-type component into the composite material used in this work, less lithium was used to achieve Li/TM < 1.25. The composition achieved for the baseline cathode in this work was $Li_{1.18}Mn_{0.53}Ni_{0.28}Co_{0.19}O_x$, where Li/TM = 1.18, suggesting a spinel component of ~6%.

Electrochemical Characterization. Slurries containing the baseline cathode material, polyvinylidene fluoride (PVDF), and C45 carbon (84:8:8) were cast on aluminum foil and dried overnight. The electrodes were calendared to 80% of the original thickness before use in cells. The active material loading was 8 mg/cm^2. Celgard polypropylene and graphite-based electrodes were used as the separator and anode, respectively, for coin cell testing. The electrolyte was 1.2 M $LiPF_6$ dissolved in ethylene carbonate/ethyl methyl carbonate (EC:EMC 3:7 by weight).

The cycling protocol used consists of an activation cycle between 4.5 and 2.0 V (vs graphite) at C/10 followed by continuous cycling between 4.4 and 2.5 V (C/2). Further details of the cycling protocol can be found elsewhere.[43] The capacity delivered during the first cycle activation between 4.5 and 2.0 V was ~215 mAh/g (not shown). In the current work, the capacity dropped to ~190 mAh/g upon limiting the voltage window to 4.4−2.5 V (~C/2) in subsequent cycles.

Scanning Electron Microscope Imaging. The morphologies of the material were investigated by scanning electron microscopy (SEM) and energy dispersive X-ray spectroscopy using a Hitachi S-4700-II microscope in the Electron Microscopy Center, Argonne National Laboratory.

X-ray Diffraction. High-energy synchrotron X-ray diffraction measurements were carried out on the LMR-NMC cathode powder at 11-BM at the Advanced Photon Source at Argonne National Lab (λ = 0.414561 Å).

Transmission Electron Microscopy. Cathode samples were scratched from the Al current collector, sonicated in IPA, drop casted onto lacy carbon grids, dried, and loaded on a double tilt TEM holder. Scanning transmission electron microscopy and electron energy loss spectroscopy were performed using a JEOL JEM-ARM200CF STEM instrument equipped with a cold field emission gun with 0.78 Å spatial resolution and a Gatan Quantom EELS detector. A 22 mrad probe convergence angle was used to perform STEM imaging. A HAADF detector with 90 mrad inner-detector angle was utilized to obtain *Z*-contrast atomic resolution images. A LAADF detector with 45 mrad inner-detector angle was utilized to obtain defect-sensitive images. The color-coded images were restructured from the atomic resolution images using Gatan Microscopy Suite (GMS3) software, in which diffraction spots from each grain were masked to generate reconstructed atomic images by the inverted FFT function. Then, images from various phases were combined to form the color-coded reconstructed images. EELS was carried out with 0.5 eV/channel dispersion on a 2048-channel EELS detector using a 5 mm detector aperture. The full width at half-maximum of the zero loss peak was measured as 0.6 eV which determines the energy resolution of the obtained spectra. EELS map acquisitions were carried out by 5 Å pixel size and 0.2 s dwell time on a 77 nm area. Electron dispersive spectroscopy (EDS) was carried out using an Oxford X-max 100TLE windowless SDD X-ray detector.

Density Functional Theory Calculations. DFT calculations[44] were performed using the Vienna Ab Initio Simulations Package (VASP)[45] code employing the generalized-gradient approximation (GGA)[46] using the PBE (Perdew, Burke, and Ernzerhof)[47] functional to account for the exchange-correlation effects. In addition, to account for the Coulombic repulsion between localized electrons in transition metals (Ni, Mn, and Co), the DFT+U schema is used. The Hubbard parameters ($U-J$) for Ni, Mn, and Co are set as 6.7, 4.2, and 5.96, respectively.[48] For systems with an even number of electrons, non-spin-polarized calculations are performed, and for systems with an odd number of electrons, unrestricted spin-polarized calculations are performed. The migration paths and barriers are determined using the linear nudged-elastic-band method, as implemented in VASP code.

For all calculations, a cutoff energy of 500 eV is used. The further increase of cutoff energy to 550 eV led to a change of the total energy of less than 0.02 eV. All structural optimizations are carried out until the forces, acting on atoms, are below 0.01 eV/Å. The criteria for energy change is set to 0.1 eV.

The $LiNi_xMn_xCo_xO_2$ (NMC) computational slab is created from the $LiCoO_2$ (LCO) unit cell, by repeating it three times through **a** and **b** vectors (Figure S3) and randomly substituting Co atoms by the appropriate amount of Ni and Mn atoms. The final NMC slab has 108 atoms and the lattice constants $a = b$ = 8.45 Å and c = 14.05 Å ($\alpha = \beta = 90°$, $\gamma = 120°$). For all of the calculations, a *k*-point mesh of 4 × 4 × 2 is used. In order to ensure that the slab size is chosen properly and represents the properties of the macroscopic crystal structure, the Li diffusion energetics is calculated for two different slab sizes. The first slab is 108 atoms, as described above, and the second one is 192 atoms. In the case of the 192-atom configuration, the Li diffusion barrier has changed less than 1% compared to the slab with 108 atoms. Thus, in order to perform computationally effective calculations, the slab with 108 atoms is used.

■ ASSOCIATED CONTENT

Ⓢ Supporting Information

The Supporting Information is available free of charge at https://pubs.acs.org/doi/10.1021/acs.nanolett.9b04620.

> The details of sample synthesis, basic characterization, and electrochemical tests and supplemental figures (PDF)

■ AUTHOR INFORMATION

Corresponding Authors

*E-mail: Croy@anl.gov.
*E-mail: rsyassar@uic.edu.

ORCID

Soroosh Sharifi-Asl: 0000-0003-0441-9231
Vitaliy Yurkiv: 0000-0002-3407-891X
Arturo Gutierrez: 0000-0002-2899-3089
Farzad Mashayek: 0000-0003-1187-4937
Jason Croy: 0000-0002-5839-3666
Reza Shahbazian-Yassar: 0000-0002-7744-4780

Author Contributions

S.S.-A., A.G., and V.Y. contributed equally to this work. S.S.-A. and R.S.-Y. initiated the idea and designed the experimental protocols. A.G., J.C., and M.B. synthesized the sample and carried out the electrochemical cycling experiments. S.S.-A. performed the STEM experiments and conducted the data analysis. V.Y. and F.M. carried out the DFT calculations. All of the authors contributed to the writing and discussion of the manuscript.

Notes

The authors declare no competing financial interest.

ACKNOWLEDGMENTS

R.S.-Y. acknowledges the financial support from the National Science Foundation (Award No. 1805938). This work made use of the JEOL JEM-ARM200CF in the Electron Microscopy Core of UIC's Research Resources Center. The acquisition of this instrument was supported by an MRI-R2 grant from the National Science Foundation (DMR-0959470). The present DFT calculations were supported by the National Science Foundation Extreme Science and Engineering Discovery Environment (XSEDE) (Award No. TG-DMR180106) as well as the Advanced Cyberinfrastructure for Education and Research (ACER) group at the University of Illinois at Chicago (URL: https://acer.uic.edu). Support from the U.S. Department of Energy, Office of Energy Efficiency and Renewable Energy, in particular from David Howell and Peter Faguy, is gratefully acknowledged. The submitted manuscript has been created by UChicago Argonne, LLC, Operator of Argonne National Laboratory ("Argonne"). Argonne, a U.S. Department of Energy Office of Science laboratory, is operated under Contract No. DE-AC02-06CH11357. The U.S. Government retains for itself, and others acting on its behalf, a paid-up, nonexclusive, irrevocable worldwide license in said article to reproduce, prepare derivative works, distribute copies to the public, and perform publicly and display publicly, by or on behalf of the Government.

REFERENCES

(1) Radin, M. D.; Hy, S.; Sina, M.; Fang, C.; Liu, H.; Vinckeviciute, J.; Zhang, M.; Whittingham, M. S.; Meng, Y. S. Narrowing the Gap between Theoretical and Practical Capacities in Li-Ion Layered Oxide Cathode Materials. *Adv. Energy Mater.* **2017**, *7*, 1602888.

(2) Qiu, B.; Zhang, M.; Xia, Y.; Liu, Z.; Meng, Y. S. Understanding and Controlling Anionic Electrochemical Activity in High-Capacity Oxides for Next Generation Li-Ion Batteries. *Chem. Mater.* **2017**, *29*, 908−915.

(3) Yan, J.; Liu, X.; Li, B. Recent Progress in Li-Rich Layered Oxides as Cathode Materials for Li-Ion Batteries. *RSC Adv.* **2014**, *4*, 63268−63284.

(4) Nayak, P. K.; Erickson, E. M.; Schipper, F.; Penki, T. R.; Munichandraiah, N.; Adelhelm, P.; Sclar, H.; Amalraj, F.; Markovsky, B.; Aurbach, D. Review on Challenges and Recent Advances in the Electrochemical Performance of High Capacity Li- and Mn-Rich Cathode Materials for Li-Ion Batteries. *Adv. Energy Mater.* **2018**, *8*, 1702397.

(5) Pan, H.; Zhang, S.; Chen, J.; Gao, M.; Liu, Y.; Zhu, T.; Jiang, Y. Li- and Mn-Rich Layered Oxide Cathode Materials for Lithium-Ion Batteries: A Review from Fundamentals to Research Progress and Applications. *Mol. Syst. Des. Eng.* **2018**, *3*, 748−803.

(6) Croy, J. R.; Balasubramanian, M.; Gallagher, K. G.; Burrell, A. K. Review of the U.S. Department of Energy's "Deep Dive" Effort to Understand Voltage Fade in Li- and Mn-Rich Cathodes. *Acc. Chem. Res.* **2015**, *48*, 2813−2821.

(7) Croy, J. R.; Gallagher, K. G.; Balasubramanian, M.; Chen, Z.; Ren, Y.; Kim, D.; Kang, S.; Dees, D. W.; Thackeray, M. M. Examining Hysteresis in Composite $x\mathrm{Li_2MnO_3}\cdot(1-x)\mathrm{LiMO_2}$ Cathode Structures. *J. Phys. Chem. C* **2013**, *117*, 6525−6536.

(8) Teufl, T.; Pritzl, D.; Mendez, M. A.; Solchenbach, S. State of Charge Dependent Resistance Build-Up in Li- and Mn-Rich Layered Oxides during Lithium Extraction and Insertion. *J. Electrochem. Soc.* **2019**, *166*, A1275−A1284.

(9) Gowda, S. R.; Dees, D. W.; Jansen, A. N.; Gallagher, K. G. Examining the Electrochemical Impedance at Low States of Charge in Lithium- and Manganese-Rich Layered Transition-Metal Oxide Electrodes. *J. Electrochem. Soc.* **2015**, *162*, A1374−A1381.

(10) Seo, D.-H.; Lee, J.; Urban, A.; Malik, R.; Kang, S.; Ceder, G. The Structural and Chemical Origin of the Oxygen Redox Activity in Layered and Cation-Disordered Li-Excess Cathode Materials. *Nat. Chem.* **2016**, *8*, 692−697.

(11) Croy, J. R.; Iddir, H.; Gallagher, K.; Johnson, C. S.; Benedek, R. First-Charge Instabilities of Layered-Layered Lithium-Ion-Battery Materials. *Phys. Chem. Chem. Phys.* **2015**, *17* (17), 24382−24391.

(12) Chen, C.-J.; Pang, W. K.; Mori, T.; Peterson, V. K.; Sharma, N.; Lee, P.-H.; Wu, S.-h.; Wang, C.-C.; Song, Y.-F.; Liu, R.-S. The Origin of Capacity Fade in the $\mathrm{Li_2MnO_3}\cdot\mathrm{Li}M\mathrm{O_2}$ (M = Li, Ni, Co, Mn) Microsphere Positive Electrode: An *Operando* Neutron Diffraction and Transmission X-ray Microscopy Study. *J. Am. Chem. Soc.* **2016**, *138*, 8824−8833.

(13) Liu, H.; Chen, Y.; Hy, S.; An, K.; Venkatachalam, S.; Qian, D. Operando Lithium Dynamics in the Li-Rich Layered Oxide Cathode Material via Neutron Diffraction. *Adv. Energy Mater.* **2016**, *6*, 1502143.

(14) Mu, L.; Lin, R.; Xu, R.; Han, L.; Xia, S.; Sokaras, D.; Steiner, J. D.; Weng, T.; Nordlund, D.; Doe, M. M.; et al. Oxygen Release Induced Chemomechanical Breakdown of Layered Cathode Materials. *Nano Lett.* **2018**, *18*, 3241−2149.

(15) Bak, S. M.; Hu, E.; Zhou, Y.; Yu, X.; Senanayake, S. D.; Cho, S. J.; Kim, K. B.; Chung, K. Y.; Yang, X. Q.; Nam, K. W. Structural Changes and Thermal Stability of Charged $\mathrm{LiNi}_x\mathrm{Mn}_y\mathrm{Co}_z\mathrm{O_2}$ Cathode Materials Studied by Combined in Situ Time-Resolved XRD and Mass Spectroscopy. *ACS Appl. Mater. Interfaces* **2014**, *6*, 22594−22601.

(16) Yan, P.; Zheng, J.; Gu, M.; Xiao, J.; Zhang, J. G.; Wang, C. M. Intragranular Cracking as a Critical Barrier for High-Voltage Usage of Layer-Structured Cathode for Lithium-Ion Batteries. *Nat. Commun.* **2017**, *8*, 14101.

(17) Yano, A.; Shikano, M.; Ueda, A.; Sakaebe, H.; Ogumi, Z. $\mathrm{LiCoO_2}$ Degradation Behavior in the High-Voltage Phase Transition Region and Improved Reversibility with Surface Coating. *J. Electrochem. Soc.* **2017**, *164*, A6116−A6122.

(18) Yan, P.; Zheng, J.; Liu, J.; Wang, B.; Cheng, X.; Zhang, Y.; Sun, X.; Wang, C.; Zhang, J. Tailoring Grain Boundary Structures and Chemistry of Ni-Rich Layered Cathodes for Enhanced Cycle Stability of Lithium-Ion Batteries. *Nat. Energy* **2018**, *3*, 600−605.

(19) Gallagher, K. G.; Croy, J. R.; Balasubramanian, M.; Bettge, M.; Abraham, D. P.; Burrell, A. K.; Thackeray, M. M. Electrochemistry Communications Correlating Hysteresis and Voltage Fade in Lithium- and Manganese-Rich Layered Transition-Metal Oxide Electrodes. *Electrochem. Commun.* **2013**, *33*, 96−98.

(20) Dogan, F.; Long, B. R.; Croy, J. R.; Gallagher, K. G.; Iddir, H.; Russell, J. T.; Balasubramanian, M.; Key, B. Re-Entrant Lithium Local Environments and Defect Driven Electrochemistry of Li- and Mn-Rich Li-Ion Battery Cathodes. *J. Am. Chem. Soc.* **2015**, *137*, 2328−2335.

(21) Singer, A.; Zhang, M.; Hy, S.; Cela, D.; Fang, C.; Wynn, T. A.; Qiu, B.; Xia, Y.; Liu, Z.; Ulvestad, A.; et al. Nucleation of Dislocations and Their Dynamics in Layered Oxide Cathode Materials during Battery Charging. *Nat. Energy* **2018**, *3*, 641−647.

(22) Lu, Z.; Chen, Z.; Dahn, J. R. Lack of Cation Clustering in $\mathrm{Li}[\mathrm{Ni}_x\mathrm{Li}_{1/3-2x/3}\mathrm{Mn}_{2/3-x/3}]\mathrm{O_2}$ $(0 < x \leq {}^1/_2)$ and $\mathrm{Li}[\mathrm{Cr}_x\mathrm{Li}_{(1-x)/3}\mathrm{Mn}_{(2-2x)/3}]\mathrm{O_2}$ $(0 < x < 1)$. *Chem. Mater.* **2003**, *15*, 3214−3220.

(23) Yan, J.; Liu, X.; Li, B. Recent Progress in Li-Rich Layered Oxides as Cathode Materials for Li-Ion Batteries. *RSC Adv.* **2014**, *4*, 63268−63284.

(24) Yu, H.; Zhou, H. High-Energy Cathode Materials ($\mathrm{Li_2MnO_3}-\mathrm{LiMO_2}$) for Lithium-Ion Batteries. *J. Phys. Chem. Lett.* **2013**, *4*, 1268−1280.

(25) Gu, M.; Belharouak, I.; Genc, A.; Wang, Z.; Wang, D.; Amine, K.; Gao, F.; Zhou, G.; Thevuthasan, S.; Baer, D. R.; et al. Conflicting Roles of Nickel in Controlling Cathode Performance in Lithium Ion Batteries. *Nano Lett.* **2012**, *12*, 5186−5191.

(26) Wen, J. G.; Bareño, J.; Lei, C. H.; Kang, S. H.; Balasubramanian, M.; Petrov, I.; Abraham, D. P. Analytical Electron

Microscopy of $Li_{1.2}Co_{0.4}Mn_{0.4}O_2$ for Lithium-Ion Batteries. *Solid State Ionics* **2011**, *182*, 98−107.

(27) Thackeray, M. M.; Kang, S. H.; Johnson, C. S.; Vaughey, J. T.; Hackney, S. A. Comments on the Structural Complexity of Lithium-Rich $Li_{1+x}M_{1-x}O_2$ Electrodes (M = Mn, Ni, Co) for Lithium Batteries. *Electrochem. Commun.* **2006**, *8*, 1531−1538.

(28) Thackeray, M. M.; Kang, S.-H.; Johnson, C. S.; Vaughey, J. T.; Benedek, R.; Hackney, S. A. Li_2MnO_3-Stabilized $LiMO_2$ (M = Mn, Ni, Co) Electrodes for Lithium-Ion Batteries. *J. Mater. Chem.* **2007**, *17*, 3112.

(29) Shukla, A. K.; Ramasse, Q. M.; Ophus, C.; Duncan, H.; Hage, F.; Chen, G. Unravelling Structural Ambiguities in Lithium- and Manganese-Rich Transition Metal Oxides. *Nat. Commun.* **2015**, *6*, 8711.

(30) Koga, H.; Croguennec, L.; Mannessiez, P.; Ménétrier, M.; Weill, F.; Bourgeois, L.; Duttine, M.; Suard, E.; Delmas, C. $Li_{1.20}Mn_{0.54}Co_{0.13}Ni_{0.13}O_2$ with Different Particle Sizes as Attractive Positive Electrode Materials for Lithium-Ion Batteries: Insights into Their Structure. *J. Phys. Chem. C* **2012**, *116*, 13497−13506.

(31) Peng, Y.; Nellist, P. D.; Pennycook, S. J. HAADF-STEM Imaging with Sub-Angstrom Probes: A Full Bloch Wave Analysis. *J. Electron Microsc.* **2004**, *53*, 257−266.

(32) Phillips, P. J.; Graef, M. De; Kovarik, L.; Agrawal, A.; Windl, W.; Mills, M. J. Atomic-Resolution Defect Contrast in Low Angle Annular Dark-Field STEM. *Ultramicroscopy* **2012**, *116*, 47−55.

(33) Long, B. R.; Croy, J. R.; Dogan, F.; Suchomel, M. R.; Key, B.; Wen, J.; Miller, D. J.; Thackeray, M. M.; Balasubramanian, M. Effect of Cooling Rates on Phase Separation in $0.5Li_2MnO_3 \cdot 0.5LiCoO_2$ Electrode Materials for Li-Ion Batteries. *Chem. Mater.* **2014**, *26*, 3565−3572.

(34) Bareno, J.; Balasubramanian, M.; Kang, S. H.; Wen, J. G.; Lei, C. H.; Pol, S. V.; Petrov, I.; Abraham, D. P. Long-Range and Local Structure in the Layered Oxide. *Chem. Mater.* **2011**, *23*, 2039−2050.

(35) Croy, J. R.; Gallagher, K. G.; Balasubramanian, M.; Long, B. R.; Thackeray, M. M. $xLi_2MnO_3 \cdot (1-x)LiMn_{0.5}Ni_{0.5}O_2$ Electrodes as a Function of Li_2MnO_3 Content. *J. Electrochem. Soc.* **2014**, *161*, A318−A325.

(36) Balasubramanian, M.; Mcbreen, J.; Davidson, I. J. In Situ X-Ray Absorption Study of a Layered Manganese-Chromium Oxide-Based Cathode Material. *J. Electrochem. Soc.* **2002**, *149*, A176−A184.

(37) Lin, F.; Markus, I. M.; Nordlund, D.; Weng, T.-C.; Asta, M. D.; Xin, H. L.; Doeff, M. M. Surface Reconstruction and Chemical Evolution of Stoichiometric Layered Cathode Materials for Lithium-Ion Batteries. *Nat. Commun.* **2014**, *5*, 3529.

(38) Yan, P.; Zheng, J.; Zheng, J.; Wang, Z.; Teng, G.; Kuppan, S.; Xiao, J.; Chen, G.; Pan, F.; Zhang, J. G.; et al. Cathode Materials: Ni and Co Segregations on Selective Surface Facets and Rational Design of Layered Lithium Transition-Metal Oxide Cathodes. *Adv. Energy Mater.* **2016**, *6*, 1−9.

(39) Gilbert, J. A.; Shkrob, I. A.; Abraham, D. P. Transition Metal Dissolution, Ion Migration, Electrocatalytic Reduction and Capacity Loss in Lithium-Ion Full Cells. *J. Electrochem. Soc.* **2017**, *164*, A389−A399.

(40) Watanabe, S.; Kinoshita, M.; Hosokawa, T.; Morigaki, K. Capacity Fading of $LiAl_yNi_{1-x-y}Co_xO_2$ Cathode for Lithium-Ion Batteries during Accelerated Calendar and Cycle Life Tests (Effect of Depth of Discharge in Charge e Discharge Cycling on the Suppression of the Micro-Crack Generation of $LiAl_yNi_{1-x-y}Co_xO_2$ Particle). *J. Power Sources* **2014**, *260*, 50−56.

(41) Hwang, S.; Kim, S. M. Y.; Bak, S. M.; Kim, S. M. Y.; Cho, B. W.; Chung, K. Y.; Lee, J. Y.; Stach, E. A.; Chang, W. Using Real-Time Electron Microscopy To Explore the Effects of Transition-Metal Composition on the Local Thermal Stability in Charged $Li_xNi_yMn_zCo_{1-y-z}O_2$ Cathode Materials. *Chem. Mater.* **2015**, *27*, 3927−3935.

(42) Yan, P.; Zheng, J.; Zhang, J. G.; Wang, C. Atomic Resolution Structural and Chemical Imaging Revealing the Sequential Migration of Ni, Co, and Mn upon the Battery Cycling of Layered Cathode. *Nano Lett.* **2017**, *17*, 3946−3951.

(43) Long, B. R.; Rinaldo, S. G.; Gallagher, K. G.; Dees, D. W.; Trask, S. E.; Polzin, B. J.; Jansen, A. N.; Abraham, D. P.; Bloom, I.; Croy, J. R.; et al. *J. Electrochem. Soc.* **2016**, *163*, A2999−A3009.

(44) Kohn, W.; Sham, L. J. Self-Consistent Equations Including Exchange and Correlation Effects. *Phys. Rev.* **1965**, *140*, A1133−A1138.

(45) Kresse, G.; Furthmüller, J. Efficient Iterative Schemes for Ab Initio Total-Energy Calculations Using a Plane-Wave Basis Set. *Phys. Rev. B: Condens. Matter Mater. Phys.* **1996**, *54*, 11169−11186.

(46) Perdew, J.; Chevary, J.; Vosko, S.; Jackson, K.; Pederson, M.; Singh, D.; Fiolhais, C. Atoms, Molecules, Solids, and Surfaces: Applications of the Generalized Gradient Approximation for Exchange and Correlation. *Phys. Rev. B: Condens. Matter Mater. Phys.* **1992**, *46*, 6671−6687.

(47) Perdew, J. P.; Burke, K.; Ernzerhof, M. Generalized Gradient Approximation Made Simple. *Phys. Rev. Lett.* **1996**, *77*, 3865−3868.

(48) Sun, H.; Zhao, K. Electronic Structure and Comparative Properties of $LiNi_xMn_yCo_zO_2$ Cathode Materials. *J. Phys. Chem. C* **2017**, *121*, 6002−6010.